# Resonance Raman Optical Activity of Single Walled Chiral Carbon Nanotubes

Péter R. Nagy,[*,†] János Koltai,[‡] Péter R. Surján,[§] Jenő Kürti,[‡] and Ágnes Szabados[§]

[†]MTA-BME Lendület Quantum Chemistry Research Group, Department of Physical Chemistry and Materials Science, Budapest University of Technology and Economics, P.O. Box 91, H-1521 Budapest, Hungary

[‡]Department of Biological Physics and [§]Laboratory of Theoretical Chemistry, Loránd Eötvös University, P.O. Box 32, H-1518 Budapest, Hungary

ABSTRACT: Resonance (vibrational) Raman Optical Activity (ROA) spectra of six chiral single-walled carbon nanotubes (SWCNTs) are studied by theoretical means. Calculations are performed imposing line group symmetry. Polarizability tensors, computed at the π-electron level, are differentiated with respect to DFT normal modes to generate spectral intensities. This computational protocol yields a ROA spectrum in good agreement with the only experiment on SWCNT, available at present. In addition to the conventional periodic electric dipole operator we introduce magnetic dipole and electric quadrupole operators, suitable for conventional k-space calculations. Consequences of the complex nature of the wave function on the scattering cross section are discussed in detail. The resonance phenomenon is accounted for by the short time approximation. Involvement of fundamental vibrations in the region of the intermediate frequency modes is found to be more notable in ROA than in Raman spectra. Calculations indicate exceptionally strong resonance enhancement of SWCNT ROA signals. Resonance ROA profile of the (6,5) tube shows an interesting sign change that may be exploited experimentally for SWCNT identification.

Raman Optical Activity

chiral carbon nanotubes
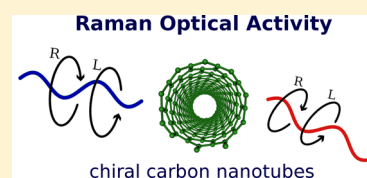
1. INTRODUCTION

As modern applications require increasingly more precise control over even the absolute configuration of single-walled carbon nanotubes (SWCNTs), significant attention has turned toward separation and characterization of chiral SWCNTs.[1,2] Large scale preparation procedures[3] yield mixtures of these nanotubes with a variety of geometrical structures, described by the so-called chiral vector (n,m).[4,5] Except for the $n = m$ (armchair) and $m = 0$ (zigzag) cases, all SWCNTs are inherently chiral, which results from the lack of mirror symmetry in their structure. Although length, diameter or even chiral vector coordinate specific samples can be prepared routinely using advanced separation methodologies, the right-handed (P) and left-handed (M) enantiomers are often present in racemic mixtures due to achiral synthetic conditions.[6]

Various solutions for enrichment in a single enantiomer emerged only recently and are still actively investigated.[7−9] Techniques under current development exploit enantiomer specific interactions between a SWCNT and a carefully designed chiral bonding agent.[9,10] Chiral complexations were carried out with DNA strands,[11] chiral polymers,[12] nano-tweezers,[13,14] and chiral surfactants[15,16] and then standard separation ideas, chromatography,[11,17] extraction,[12−14,18] and ultracentrifugation[15,16] yielded optically active SWCNT samples. Bottom-up approaches like chemical synthesis[19] and specific SWCNT templated selective nanotube growth[20,21] represent promising alternatives to gain ultimate experimental control over SWCNT structure.

Raman spectroscopy is a standard tool of SWCNT characterization; it is, however, blind to chiral information as per se. There are only a limited number of studies on SWCNT optical activity. Most of these consider electronic circular dichroism spectroscopy, either from the experimental[7,12−16,22−24] or from the theoretical side.[25−28] Raman optical activity (ROA) is an emerging, alternative chiroptical technique for chiral SWCNT characterization. To the best of our knowledge, our previous work was the first theoretical study on SWCNT resonance ROA (RROA).[29] The recently reported study of Magg et al.[30] is the first experiment in this line. Let us note for completeness that handedness of an individual SWCNT can also be investigated by scanning probe microscopy[31,32] and transmission electron microscopy.[33]

The present work is concerned with theoretical description of the vibrational RROA phenomenon for SWCNTs. In the RROA process either the incident or the Raman scattered photon is in resonance with an electronic transition of the system. Optical activity accompanies inelastic light scattering, which involves a vibrational transition.[34] In the most frequent arrangement of $SCP_U(180°)$-ROA, backscattered circular polarized (SCP) light is measured originating from an unpolarized (U) incident laser beam. ROA is an excellent complementary method to electronic circular dichroism, as it samples the numerous vibrations of the system, often revealing a wealth of structural information.[34−36] Regarding that some of the well-established techniques for SWCNT characterization are based on the Raman effect,[37] e.g., single nanotube

spectroscopy, the related optical activity spectroscopy may gain special significance in the future.

In lack of experiment our previous theoretical work suggested that the (6,5) tube exhibits exceptionally large RROA signal at the experimentally most relevant 532 nm incident light wavelength. Recently, Magg et al.[30] proved that RROA is indeed measurable in spite of experimental challenges, such as small enantiomeric excess and small sample concentration. In the experiment of Magg et al. enhancement of the ROA intensity originates in the resonance between Stokes-shifted photons and the second electronic transition of the (6,5) nanotube.[30]

Computations are indispensable for assigning ROA spectra. Spectrum simulation essentially involves the calculation of spectral line positions (i.e., vibrational frequencies) and line intensities. Vibrational normal modes are usually obtained within the harmonic approximation. This step of the computation represents the bottleneck in the case of large (finite) molecules[38] or periodic systems with large unit cells. Iterative subspace techniques[39,40] or linear scaling evaluation of the molecular Hessian[41] might change this trend in the near future. In this work the helical symmetry of the chiral SWCNTs was partially exploited to make the normal mode computation manageable.[42,43]

Simulation of spectral intensities necessitates computation derivatives of ROA polarizability tensors with respect to the normal coordinates.[34,44] In this regard, relying on the linear response of single determinantal models [either Hartree–Fock or Kohn–Sham density functional theory (DFT)][38,44,45] has been found sufficient in most cases for reproducing experimental intensities.[46–50] Approximate methods based on the fragmentation of a large molecule[51–53] extended the size of reachable systems significantly but are inapplicable to the indivisible delocalized π-electron system of the nanotubes. One cannot rely on efficient ab initio ROA implementations[38,54,55] for modeling nonfinite SWCNTs either, for the following reasons: (i) lack of ROA polarizability tensor expressions suitable for periodic systems; (ii) cost-efficient treatment of resonance is rarely available;[55] (iii) restrictions to real valued wave functions and corresponding purely real or imaginary polarizability tensors.

These limitations are overcome in our present implementation by (i) introducing a formula for the magnetic dipole and the electric quadrupole operators that is periodic (i.e., commutes with translational operators) in analogy with the well-known expression for the periodic electric dipole operator,[56] applied frequently, e.g., for simulating Raman spectra of periodic systems.[57–59] Regarding (ii), we adopt the short time approximation of Jensen et al.[55] to account for the resonance phenomenon. Considering (iii), genuinely complex ROA polarizability derivatives are evaluated with complex, (translationally) periodic wave functions. Scattering cross section expressions, valid in the case of complex polarizability tensors, as formulated according to the general ROA theory of Nafie,[34,60,61] are implemented.

Similarly to our previous studies,[29,62] spectral cross sections are computed at the π-electron level, whereas structure optimization and vibrational modes are obtained with DFT. This computational protocol was validated by comparison to experimental Raman and accurate theoretical ROA spectra of common chiral fullerenes, such as C_{76} and C_{84}.[29,62] For systems with just slightly curved surface, like C_{76} or C_{84}, a tight-binding (TB) approximation at the π-electron level already gives

qualitatively good spectra, which has been adopted for a periodic RROA computation previously.[29] The TB model of ref 29 was improved here in two regards, the so-called band polarization terms (Appendix B) were included and a simple level-shift is added to the one-particle energies, which correction was successful in the case of C_{76} in ref 62.

In what follows we first give a comprehensive account of the theoretical approach underlying our calculations. In section 2 the selected π-electron model and the computation of spectral intensities are introduced briefly, but the focus is kept on features that have not been discussed previously[29,62] and that are necessary for treating periodic systems. These theoretical advancements were partly implied but not dwelled on in our previous report.[29] Our novel applications are presented in section 3, giving RROA spectra for six chiral SWCNTs with relatively small diameters. Our previous report resorted to the three most important fundamental modes of the (6,5) tube, and we now account for all fundamental vibrations. Note that defect-induced bands, bands originating from higher order scattering processes, etc. that appear in experimental Raman spectra are not considered in the present study. Besides simulating RROA spectra, we compute dependence of the ROA signal on the incident laser frequency for some spectral bands.

2. THEORY

2.1. Model Hamiltonian. A symmetry-adapted version of the tight-binding (TB) π-electron model, introduced in our previous reports,[29,62,63] is applied presently. Elements of the model are briefly recapitulated for completeness. The present TB model is a Hückel-type π-electron model that is periodic symmetry adapted and its first-neighbor interaction terms are bond-length dependent so that derivatives with respect to Cartesian coordinates can be formulated.

Notation $k \in [-\pi/a, \pi/a]$ is adopted for the irreducible representations of the translational group (k is the so-called quasi-momentum). We assume that a quasi-one-dimensional system is aligned parallel with axis z and the lattice constant is denoted by a.

The field-independent Hamiltonian is given as

$$\hat{H} = \int dk \sum_{\mu\nu} H_{\mu\nu}(k) \sum_{\sigma} \hat{a}_{\mu\sigma}^{+}(k)\, \hat{a}_{\nu\sigma}(k) \tag{1}$$

where σ stands for the spin-index and operators $\hat{a}_{\mu\sigma}^{+}(k)$ $(\hat{a}_{\nu\sigma}(k))$ create (annihilate) the so-called Bloch orbitals, $\phi_\mu(k,\mathbf{r})$. Orthonormalized orbitals (one centered on each carbon atom), denoted by $\chi_\mu(\mathbf{r})$, are used to generate elements of the orthonormal translational symmetry adapted basis according to

$$\phi_\mu(k,\mathbf{r}) = \sqrt{\frac{a}{2\pi}} \frac{1}{\sqrt{2N+1}} \sum_{n=-N}^{N} e^{inka} \hat{T}_{na} \chi_\mu(\mathbf{r}) \tag{2}$$

Operator $\hat{T}_{na}$ translates with $n \cdot a$ in direction z and $\mu = 1, ..., 2q$ with $2q$ standing for the number of atoms in the reference cell. (The analogues of AO $\chi_\mu(\mathbf{r})$ in the neighboring unit cells of the reference one will be referred to as $\chi_{\mu-2q}(\mathbf{r}) = \hat{T}_a^{-1}\chi_\mu(\mathbf{r})$ and $\chi_{\mu+2q}(\mathbf{r}) = \hat{T}_a\chi_\mu(\mathbf{r})$, respectively.) N denotes the number of unit cells that tends to infinity when the thermodynamic limit is taken.

Due to the nearest neighbor approximation, the lattice sum for $H_{\mu\nu}(k)$ takes the particularly simple form

$$H_{\mu\nu}(k) = e^{-ika} h_{\mu,\nu-2q} + h_{\mu,\nu} + e^{ika} h_{\mu,\nu+2q} \tag{3}$$

with the so-called hopping integral

$$h_{\mu,\lambda} = -h_0 e^{-\zeta R_{\mu\lambda}}$$

involving two parameters, h_0 and ζ, which are fitted to experimental excitation energies of ethylene and polyacetylene.[64,65] In the above, $R_{\mu\lambda}$ stands for the bond length. Note that $h_{\mu,\lambda}$ is nonzero only if sites μ and λ are first neighbors.

Diagonalization of the TB model Hamiltonian yields the bands $[\varepsilon_i(k)]$ and the corresponding crystal orbitals (COs):

$$\varphi_i(k,\mathbf{r}) = \sum_{\mu} C_{\mu i}(k) \, \phi_{\mu}(k,\mathbf{r}) \tag{4}$$

2.2. Spectral Intensities. When periodic symmetry is assumed, spectral line intensities are more involved than in the case of finite systems. This subject, merely mentioned previously,[29] is addressed here in detail.

The SWCNTs of our interest exhibit their second excitation energy around 2 eV, lying close below commonly applied experimental incident frequencies (e.g., 532 nm = 2.33 eV). This calls for a ROA formulation suitable for resonance. Explicit treatment of vibronic transitions[66−68] is out of question due to the large number of states to be considered. For this reason we account for the resonance by applying the short time approximation (STA).[55] Polarizabilities[35,55] needed for the scattering cross sections of Raman and ROA processes within the STA are similar to the formulas valid in the far from resonance case. The chief difference is the appearance of a damping parameter, Γ that is related to the lifetime of a virtual excited state in a reciprocal manner. For the sake of simplicity, we resort to investigating the Stokes process.

Assuming a single determinant model for a quasi-one-dimensional system exhibiting translational symmetry, a general expression for polarizabilities within the STA[29,63] is given by

$$\tau_{\alpha\beta}[d_\alpha, V_\beta] = 2 \int \sum_j^{occ} \sum_a^{virt} \left(\frac{(d_\alpha)_{ja}(k)(V_\beta)_{aj}(k)}{\omega_{aj}(k) - \omega - i\Gamma} \right.$$
$$\left. + \frac{(V_\beta)_{ja}(k)(d_\alpha)_{aj}(k)}{\omega_{aj}(k) + \omega + i\Gamma} \right) dk \tag{5}$$

which is the extension of the STA polarizability expression of ref 55 to the periodic case. Indices j (a) refer to occupied (virtual) COs and ω denotes the frequency of the incident light ($\hbar = 1$). The orbital energy difference is denoted by $\omega_{aj}(k) = \varepsilon_a(k) - \varepsilon_j(k)$ for a given k value. Greek indices α, β, γ, ... stand for Cartesian components. Finally, V_β is a unified notation for multipole moments. Choosing the electric dipole (d_β) for V_β in eq 5 gives the electric dipole−electric dipole polarizability ($\alpha_{\alpha\beta}$), substituting the magnetic dipole (m_β) for V_β leads to the electric dipole−magnetic dipole polarizability ($G_{\alpha\beta}$), whereas using the electric quadrupole ($\Theta_{\overline{\beta}} = \Theta_{\beta\gamma}$) as V_β generates the electric dipole−electric quadrupole polarizability ($A_{\alpha\overline{\beta}}$). (For transparency, hyperindex $\overline{\beta} = \beta\gamma$ is simply denoted by β when used with V.)

Orientational averaging leads to certain combinations of polarizability tensor matrix elements, the so-called invariants.[34,60] Using the symmetric and antisymmetric part of τ

$$\tau_{\alpha\beta}^S = (\tau_{\alpha\beta} + \tau_{\beta\alpha})/2 \tag{6}$$

$$\tau_{\alpha\beta}^A = (\tau_{\alpha\beta} - \tau_{\beta\alpha})/2 \tag{7}$$

the invariants are expressed as[34,61]

$$s(\alpha)^2 = \frac{1}{9}(\alpha_{\alpha\alpha})^S(\alpha_{\beta\beta})^{S*} = \frac{1}{9}\,\mathrm{Tr}(\boldsymbol{\alpha}^S)^2 \tag{8}$$

$$\beta_S(\alpha)^2 = \frac{3}{2}(\alpha_{\alpha\beta})^S(\alpha_{\alpha\beta})^{S*} - \frac{1}{2}\,\mathrm{Tr}(\boldsymbol{\alpha}^S)^2 \tag{9}$$

$$\beta_A(\alpha)^2 = \frac{3}{2}(\alpha_{\alpha\beta})^A(\alpha_{\alpha\beta})^{A*} \tag{10}$$

$$\beta_S(G)^2 = \mathrm{Im}\left\{ \frac{3}{2}(\alpha_{\alpha\beta})^S(G_{\alpha\beta})^{S*} - \frac{1}{2}\,\mathrm{Tr}(\boldsymbol{\alpha}^S)\,\mathrm{Tr}(\mathbf{G}^{S*}) \right\} \tag{11}$$

$$\beta_S(A)^2 = \frac{1}{2}\omega\,\mathrm{Re}\{(\alpha_{\alpha\beta})^S(\epsilon_{\alpha\gamma\delta}A_{\gamma,\delta\beta})^{S*}\} \tag{12}$$

$$\beta_A(A)^2 = \frac{1}{2}\omega\,\mathrm{Re}\{(\alpha_{\alpha\beta})^A[(\epsilon_{\alpha\gamma\delta}A_{\gamma,\delta\beta})^{A*} + (\epsilon_{\alpha\beta\gamma}A_{\delta,\gamma\delta})^{A*}]\} \tag{13}$$

where $\epsilon_{\alpha\beta\gamma}$ is the Levi−Civita symbol.

For real valued orbitals, $\alpha_{\alpha\beta}^A = 0$ leads to a simplification of the above invariants,[55] as a matter of fact $\beta_A(\alpha)^2 = \beta_A(A)^2 = 0$. For infinite systems, $\alpha_{\alpha\beta}^A$ does not vanish, as a consequence of basis functions of eq 2 being complex valued. The appearance of antisymmetric invariants complicates the theory on one hand; on the other hand it offers an enrichment of experimental observables. So far, symmetric invariants have been sufficient for computing ROA spectral intensities of finite molecules within the far from resonance approximation or STA.[34] Contribution of the antisymmetric invariants might be detectable for the first time for periodic systems. By variation of experimental conditions, it may even become possible to deduce the value of $\beta_A(A)$ itself and compare it to theoretical results, which could provide further verification of the so far only theorized levels of ROA description.[69,70]

Cross sections for the $\mathrm{SCP_U}(180°)$ experimental arrangement are finally expressed as[34,61]

$$d\sigma_u^{\mathrm{Raman}}(180°) = K_p[90s(\alpha^p)^2 + 14\beta_S(\alpha^p)^2 + 10\beta_A(\alpha^p)^2] \tag{14}$$

$$\Delta d\sigma_u^{\mathrm{ROA}}(180°) = \frac{4K_p}{c}[12\beta_S(G^p)^2 + 4\beta_S(A^p)^2 + 2\beta_A(A^p)^2] \tag{15}$$

with $K_p = (1/2\omega_p)(1/90)(\mu_0/(4\pi))^2(\omega - \omega_p)^3\omega$. Here, μ_0 stands for the permeability of vacuum, c denotes the speed of light and ω_p is the harmonic vibrational frequency of normal mode p. Upper index p refers to polarizability derivative, computed with respect to normal mode Q_p, taken at the equilibrium geometry, i.e.

$$\tau_{\alpha\beta}^p = \left(\frac{\partial \tau_{\alpha\beta}}{\partial Q_p} \right)_0 \tag{16}$$

2.3. Periodic Multipole Moments. Working with periodic symmetry necessitates to revise not only spectral intensities but also multipole moments. Multipole operators used commonly for finite systems lead to aperiodic, occasionally ill-defined matrix elements for periodic systems.[71−73] Difficulties originate

in the system being infinitely extended. For an infinite system, the concept of multipoles itself, arising as low order terms of a Taylor expansion with respect to the spatial coordinate, becomes questionable.

We adopted in ref 29 and apply here an approach where all operators describing light-matter interaction exhibit translational symmetry. This facilitates relying on multipoles as long as the wavelength of the incident light is orders of magnitude larger than the lattice constant, which condition is fulfilled for the 532 nm incident light. Once the translational symmetry adapted multipoles are formulated, conventional k-space considerations can be used to simulate ROA spectra.

In this section the multipole operators underlying our study are presented briefly. Of the three multipoles necessary for ROA spectral intensities, the electric dipole received by far the most consideration under the periodic boundary condition. Our notion that any form of the electric quadrupole and the magnetic dipole operators, applicable for periodic systems is not available in the literature is confirmed by a recent review.[74]

Reformulation of the conventional coordinate operator of $\hat{\mathbf{r}}$, assuming that it is acting on a lattice periodic function, has been known for long[71−73] as

$$\hat{\mathbf{r}} = ie^{i\mathbf{k}\hat{\mathbf{r}}}\hat{V}_k e^{-i\mathbf{k}\hat{\mathbf{r}}} - i\hat{V}_k \tag{17}$$

with $\hat{V}_k = \left(\frac{\partial}{\partial k_x}, \frac{\partial}{\partial k_y}, \frac{\partial}{\partial k_z}\right)$. In the field of quantum chemistry, it was Otto[56] who first considered eq 17 for periodic systems, resorting to the first term on the right-hand side, arguing that this term conserves translational symmetry. The translational symmetry adapted coordinate

$$\hat{\mathcal{R}} = ie^{i\mathbf{k}\hat{\mathbf{r}}}\hat{V}_k e^{-i\mathbf{k}\hat{\mathbf{r}}} = \hat{\mathbf{r}} + i\hat{V}_k \tag{18}$$

has become the cornerstone of many linear response based implementations for molecular property computation[75−78] since then. It has been established on the basis of the vector potential method[79,80] as well as in the framework of the modern theory of polarization[81,82] that the electric dipole corresponding to operator $\hat{\mathcal{R}}$ of eq 18 indeed describes the interaction between the homogeneous electric field and a translationally periodic system.

We proceed now by formulating a magnetic dipole and an electric quadrupole showing periodic symmetry, in analogy with the line of thought presented by Otto.[56] The present approach can be interpreted as omission of any polarization current induced by the second term on the right-hand side of eq 17, as the electromagnetic field is relatively weak and the band gap is nonzero.[56,83] Using a similar, somewhat heuristic argument, in which only the periodically symmetric terms are kept, Wannier formulated[72] the following expression for the vector potential in the periodic case:

$$\hat{A}(\mathbf{r}) = \frac{1}{2}\mathbf{B} \times (\hat{\mathbf{r}} + i\hat{V}_k) = \frac{1}{2}\mathbf{B} \times \hat{\mathcal{R}} \tag{19}$$

with $\mathbf{B}$ being the field strength of the homogeneous magnetic field. (Here and in the following atomic units are used, thus $\hbar = 1$, $e = 1$, and $m_e = 1$.) Subjecting the perturbation of $\hat{\mathbf{p}}\cdot\hat{A}(\mathbf{r})$ corresponding to $\mathbf{B}$ to simple manipulations, one can recognize a translationally periodic magnetic dipole operator:

$$\hat{\mathbf{p}}\cdot\left(\frac{1}{2}\mathbf{B} \times \hat{\mathcal{R}}\right) = \mathbf{B}\cdot\left(\frac{1}{2}\hat{\mathcal{R}} \times \hat{\mathbf{p}}\right) = -\mathbf{B}\cdot\hat{\mathcal{M}} \tag{20}$$

Note that the same operator is obtained, if the translationally symmetric coordinate, $\hat{\mathcal{R}}$ is substituted to the usual expression of the magnetic dipole operator:

$$\hat{\mathcal{M}} = -\frac{1}{2}\hat{\mathcal{R}} \times \hat{\mathbf{p}} \tag{21}$$

Operator $\hat{\mathcal{M}}$ is clearly periodic, because both $\hat{\mathcal{R}}$ and $\hat{\mathbf{p}}$ commute with $\hat{T}_{na}$. Further justification of eq 21 is provided on the grounds of the modern theory of orbital magnetization (MTOM).[84,85] As presented in Appendix A, orbital magnetization computed with $\hat{\mathcal{M}}$ is equivalent to the MTOM expression for nonmetallic systems.

Analogously, the traceless quadrupole moment, expressed with the translationally invariant coordinate, $\hat{\mathcal{R}}$ reads

$$\hat{\mathcal{T}}_{\alpha\beta} = -\frac{3}{2}\hat{\mathcal{R}}_\alpha\hat{\mathcal{R}}_\beta + \delta_{\alpha\beta}\frac{1}{2}\sum_\lambda \hat{\mathcal{R}}_\lambda^2 \tag{22}$$

Expression of eq 22 obviously commutes with $\hat{T}_{na}$.

Matrix elements of the above periodic multipole operators with COs, necessary to evaluate eq 5, are collected in Appendix B. Note that in the case of SWCNTS the reformulation of eq 18 affects only coordinate z and the related components of the magnetic dipole and electric quadrupole. Coordinates x and y remain unaffected, our system being quasi-one-dimensional.

For the sake of completeness we note that a velocity based formulation offers an alternative route to compute spectroscopic properties of periodic systems. Utilizing the equation of motion (EOM) for periodic systems:[86]

$$\hat{\mathbf{p}} = i[\hat{H},\hat{\mathcal{R}}] = i[\hat{H},ie^{i\mathbf{k}\hat{\mathbf{r}}}\hat{V}_k e^{-i\mathbf{k}\hat{\mathbf{r}}}] \tag{23}$$

and considering eigenfunctions of the Hamiltonian (nondiagonal) matrix elements of the coordinate can be expressed via matrix elements of the momentum, the latter being obviously translationally invariant. The simplicity of this approach has motivated many implementations.[86−88] However, relying on the velocity formulation has several drawbacks. Molecular properties based on the velocity or length (i.e., coordinate operator) formulation might differ significantly with noncomplete basis sets.[86] Moreover, if the model Hamiltonian does not commute with $\hat{\mathbf{r}}$ (e.g., involves exact Hartree−Fock exchange), use of the periodic coordinate operator cannot be avoided.[89,90]

3. RESULTS AND DISCUSSION

3.1. Computational Details. The above presented Raman and ROA theory applicable for semiconductor SWCNTs is implemented in our own program. We discuss here the most important aspects of computations and refer to our previous reports[29,62,63] for further details.

Raman and ROA spectra were simulated for six semiconducting, chiral SWCNTs, with chiral indices[4,91] (6,5), (7,5), (11,1), (9,5), (11,4), and (13,2). We considered P type handedness[25] for all the tubes, which corresponds to the (−) enantiomer in the case of (6,5). Diameter of the tubes studied lies in the range 7.5−11.0 Å; their curvature is, therefore, comparable to or smaller than the curvature of C_{76} and C_{84}. Large curvature may induce ill effects in the present theoretical approach, because it has been demonstrated that second and further neighbor interactions are not negligible[92] in that case. It has also been shown that the ROA spectrum computed at the TB level is prone to significant errors in the extreme case of

Table 1. Vibrational Frequencies of the Three Most Important One-Dimensional (RBM, G⁻, G⁺) and the 11 Doubly Degenerate (irrep E) Fundamental Vibrational Modes of the (6,5) SWCNT in cm⁻¹ Units Computed with the ETB[105] Method and the Presently Applied LDA Approach (Section 3.1)

modes	RBM								G⁻			G⁺		
LDA	79	189	316	355	429	650	846	861	1525	1549	1563	1592	1594	1600
ETB	86	213	294	397	407	616	874	881	1521	1575	1548	1568	1588	1570

C$_{28}$.[62] For this reason we have selected nanotubes similar in diameter to the model fullerenes for which the computational protocol was tested successfully.[29,62,63]

A specific feature of our treatment is that the π-electron model of section 2 is used for calculating spectral intensities, whereas geometry optimization and the computation of dynamical (Hessian) matrix elements is carried out at the density functional level of theory. The VASP program package[93] was applied for the latter utilizing the local density approximation (LDA) with the projector augmented wave method, 400 eV plane wave energy cutoff and a $1 \times 1 \times 5$ γ point centered Monkhorst–Pack set of k-points. For further details see refs 42 and 43.

To reduce computational effort, normal modes of carbon nanotubes in their translational unit cell are calculated with imposing helical symmetry. The translational unit cell of a nanotube, containing $2q$ atoms, can be built from two carbon atoms in its helical unit cell using rotations and screw axis symmetry operations.[94,95] Analogously, instead of calculating all elements of the $6q \times 6q$ force constant matrix, it is sufficient to compute a $6 \times 6q$ part of the Hessian describing the interaction of the two atoms in the reference helical cell with all atoms in the translational unit cell. Finally, one can apply the above symmetry operations to construct the $6q \times 6q$ dynamical matrix[43,96,97] and to assign the resulting normal modes (of the translational unit cell) to the irreducible representations in the helical line group.[94,95]

On the basis of these helical symmetry considerations,[94,95,98–100] 26 Raman and ROA active fundamental vibrations were identified in the previous work of Rusznyák et al.,[96] prior to the evaluation of the polarizability tensors here. The assignment of the theoretical spectra on Figures 1 and 3 were performed by utilizing these symmetry considerations. Among these 26 modes the RBM, G⁻, and G⁺ have been the most relevant experimentally.[4,5] The RBM mainly consists of radial movement of the carbon atoms perpendicular to the SWCNT cylinder. The G⁻ and G⁺ modes originate from the in-plane vibrations of graphene and consist mainly of in plane stretching perpendicular and parallel, respectively, to the axis of the SWCNT. The remaining one one-dimensional and 11 pairs of doubly degenerate fundamental modes, lying in the region of the so-called intermediate frequency modes (IFM),[101–104] have been less frequently observed.[105] Let us note that only the fundamental IFMs are studied here, the combinational or defect induced modes of the IFM region are not considered presently.

Polarizability derivatives, cf. eq 16, are computed by numerical differentiation with respect to only the 26 Raman and ROA active normal coordinates. For cost efficiency, numerical differentiation is preferable to analytical derivatives as only $26 \cdot 2 + 1 = 53$ different polarizabilities are to be computed in the case of a three-point numerical procedure. At contrast with this, the analytical treatment requires differentiation with respect to all Cartesian coordinates of all atoms in the translational unit cell, even if only 26 normal modes are to be considered eventually.

Scattering cross sections were evaluated at the incident light frequency of 532 nm, relatively close to resonance in the case of all six SWCNTs. A system-independent damping parameter, $\Gamma = 40.8$ meV (=1.5 mE$_h$) was applied in all presented computations. This choice is close both to the experimentally and computationally obtained value of 30–50 meV broadening[106–108] for SWCNTs lying in the same diameter range as our structures.

Following the protocol established previously in the case of fullerenes,[62] excitation energies of the present TB model are shifted so that the resulting lowest unoccupied-highest occupied CO energy difference of the TB model ($\omega_{LH}(k)$) without the level shift matches the experimental first excitation energy (E_{11})[109,110] of the given nanotube. The final expression for the denominators in eq 5 accordingly reads

$$\omega_{aj}(k) + (E_{11} - \omega_{LH}(k)) \pm \omega \pm i\Gamma \qquad (24)$$

Let us note that this correction was not yet applied in our previous RROA study.[29]

Integration over the Brillouin zone is carried out numerically utilizing the Monkhorst–Pack scheme.[111] Numerical tests indicated relatively fast convergence of the Raman/ROA cross sections with the number of integration grid points, N_k (i.e., spectra obtained with $N_k = 21$ could not be distinguished from that of $N_k = 61$). For this reason $N_k = 21$ was applied in all examples.

Raman and ROA cross sections for a given vibrational frequency are depicted as Lorentzian curves with 5 cm⁻¹ line width. The spectral regions (e.g., Figure 1) are split into two intervals to allow for better perceptibility of the less intense spectral bands in the smaller wavenumber region. Visual comparison is further assisted by normalizing areas below spectral curves separately for the split intervals. Relative normalization factor (f), shown in figure labels as "xf" for each interval and nanotube type, gives the ratio of the areas under the spectral curve of (11,4) and of the actual nanotube.

3.2. Resonance Raman Spectra. We begin the analysis with the comparison of TB and experimental SWCNT Raman spectra to assess the accuracy of our computational method.

Spectral peak positions in the case of the (6,5) tube being 316, 1549, and 1594 cm⁻¹ for the (RBM, G⁻, G⁺) vibrations agree well with the recent experimental data[30,105] of 309, 1526–1528, and 1589 cm⁻¹. Regarding the remaining modes besides RBM, G⁻, G⁺, their LDA frequencies are compared in Table 1 to recent theoretical (extended tight-binding, ETB) results as experimental information is only available for a couple of these transitions,[101–104] whereas the ETB results were computed for all vibrations of our interest. The two sets of computed data in Table 1 agree within 30–40 cm⁻¹. This is acceptable, based on the fact that ETB results match measured frequencies within 20–30 cm⁻¹, when the experimental values are available,[105] and the quality of LDA and ETB frequencies are comparable in the case of RBM, G⁻, and G⁺.

Computed intensities are displayed in Figure 1, showing Raman spectra of the six selected SWCNTs. The three most
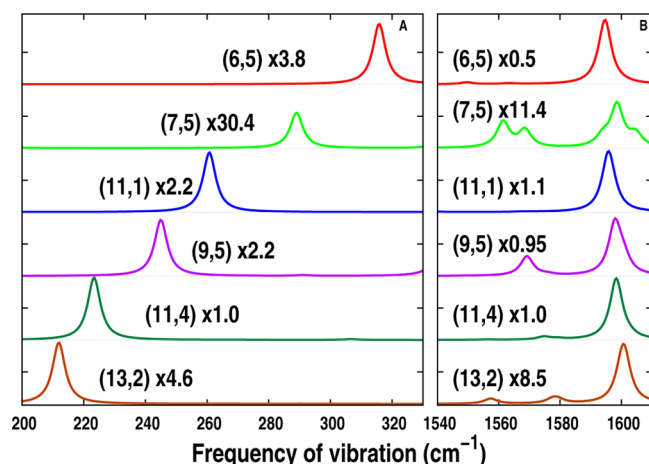
Figure 1. Unpolarized backscattering Raman cross sections of selected SWCNTs at 532 nm. Spectra of panel A are normalized over the wavenumber interval [0, 800] cm^{-1}, panel B over [800, 1800] cm^{-1}. Relative normalization factors are computed with respect to the spectrum of (11,4). See text for further notations.

intense vibrational transitions can be recognized at first sight: the strongly diameter-dependent RBM in panel A and the G$^-$ and G$^+$ modes in panel B, the latter around 1600 cm^{-1}. (For most cases IFMs are an order of magnitude less intense than the RBM and G modes and can only be observed in Figure 1 in the cases of (7,5) and (13,2). The intensities of the IFMs are comparable for all six examples; the reason for their appearance on the (7,5) and (13,2) spectra is that the intensity of their G$^+$ mode is at least an order of magnitude weaker compared to the G$^+$ intensity of the other four selected nanotubes.)

The intensity ratio for RBM, G$^-$, and G$^+$ in the case of the (6,5) tube is 1/144:1/16:1 by the present TB approach, in qualitative agreement with the experimental trend (the same ratio is approximately 1/70:1/7:1[30]), though the intensity of the RBM and G$^-$ is underestimated compared to G$^+$. This parallels the previous finding[29,62] on the reliability of the absolute intensity values of the present TB model; i.e., the more stretching character a vibration exhibits, the better the electron–phonon coupling is described. The intensity of vibrations with significant bending or torsion component is less satisfactory than those being essentially stretching modes. Because bending and torsion character increases in the sequence G$^+$, G$^-$, and RBM, we expect the TB intensity of G$^+$ to be the most reliable, whereas the intensity of the RBM is probably the most underestimated by our model.

As relative normalization factors shown in Figure 1 reflect, Raman intensities are highly sensitive to excitation energies of the given SWCNT. Excitation energies and spectral intensities displayed for the G$^+$ band in Table 2 supplement this information to rationalize the occasional orders of magnitude change in the intensity. Exceptionally large amplification occurs for nanotubes with electronic transitions close to 2.3 eV (c.f. E_{22} and E_{33} in Table 2).

Resonance amplification depends strongly on the incident light frequency. This effect is illustrated by Figure 2, showing the intensity as a function of ω, the so-called resonance profile, on the example of the RBM, G$^+$, and G$^-$ modes of the (6,5) tube.
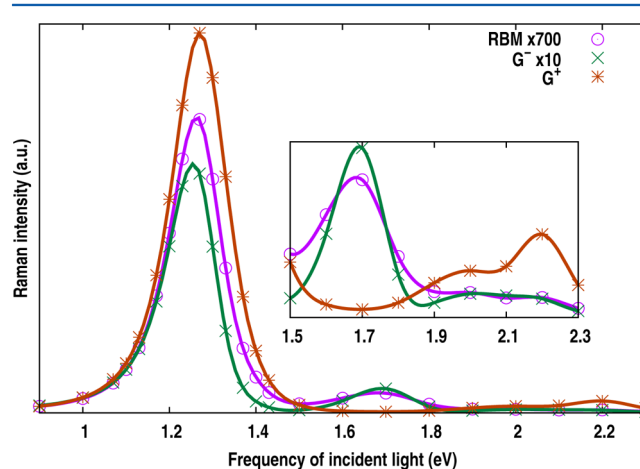
Figure 2. Resonance Raman profile of SWCNT (6,5) using the TB approximation. The RBM intensity is scaled by a factor of 700, and G$^-$ is multiplied by 10 to match the magnitude of G$^+$.

The largest intensity increase due to resonance is observed around 1.26−1.27 eV, in good agreement with the experimental value of the first electronic excitation energy,[115] as a trivial consequence of the level shift introduced in eq 24. A zoom into the tail of the curves, displayed in the inset of Figure 2, shows two additional maxima. The peak around 2.2 eV is in accordance with the second electronic transition energy assessed by the density of states computed on the basis of the (level shifted) TB model, as well as with the experimental value of E_{22} = 2.19 eV. The position of the peak in the middle, around 1.7 eV, corresponds to the difference between the first and second Van Hove peaks of the density of states (1.71 eV) in agreement with the experimentally observed E_{12} = 1.73 eV

Table 2. Relative Maxima of Raman and ROA Intensities of the G$^+$ Band by the TB Method Relative to the Intensity of the Most Intense Band (at 3194 cm^{-1}) of the Routinely Measured Organic Molecule, Methyloxirane[112] [a]

SWCNT	diameter (Å)	2q	E_{11} (eV)	E_{22} (eV)	E_{33} (eV)	Raman	ROA
(6,5)	7.5	364	1.27	2.19	3.60	3.2×10^8	4.1×10^9
(7,5)	8.2	436	1.21	1.93	3.68	9.7×10^6	2.9×10^8
(11,1)	9.0	532	0.98	2.03	2.88	1.4×10^8	3.2×10^9
(9,5)	9.6	604	1.00	1.85	3.05	4.2×10^8	5.7×10^9
(11,4)	10.5	724	0.90	1.74	2.78	1.6×10^8	4.5×10^8
(13,2)	11.0	796	0.95	1.44	3.08	1.1×10^7	2.1×10^8

[a]Nonresonance (ω = 532 nm) methyloxirane spectra are computed by the G09 program package,[113] utilizing the B3LYP density functional and the aug(sp)-cc-pVDZ basis.[54] Geometrical parameters of the SWCNTs are taken from the database of Rusznyák et al.[114] Experimental electronic excitation energies E_{11}, E_{22}, and E_{33} are collected from refs 109 and 110. The number of atoms in the translational unit cell is denoted by 2q. See text for further details.

transition. The $1 \rightarrow 2$ transition requires circularly polarized light with nonzero perpendicular component to the tube axis,[116] which is also allowed in our case. On the basis of Figure 2, approximately 1000 nm laser frequency is the optimal choice for the largest amplification by resonance.

The above findings allow to shortly conclude that the TB Raman spectra is in qualitative agreement with experimental and theoretical data available in the literature.

3.3. Resonance ROA Spectra. Comparing the TB ROA spectrum for the (6,5) tube, depicted in Figure 3, with the
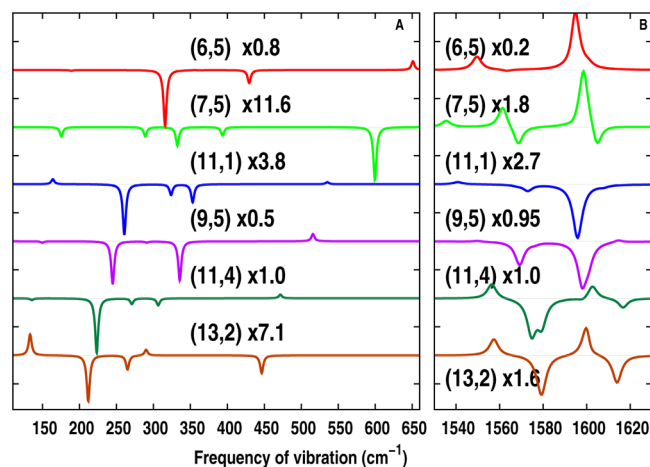
Figure 3. Unpolarized backscattering ROA cross sections of selected SWCNT at 532 nm. Spectra of panel A are normalized over the wavenumber interval $[0, 800]$ cm^{-1}, panel B over $[800, 1800]$ cm^{-1}. Relative normalization factor values are computed with respect to the spectrum of (11,4). See text for further notations.

recent measurement of Magg et al.,[30] the sign of the G modes as well as the intensity ratio 1:5 of G$^-$ and G$^+$ match the experiment perfectly. Experiment and theory are also in accord in the RBM being much less intense than G$^+$, their intensity ratio of 1:83 compares to the ca. 1:100 value of the experiment.

Regarding the sign of RBM, the theoretical and experimental spectra are in contradiction. The source of this discrepancy might be either the approximate nature of our model or experimental difficulties or both and deserves further investigation.

Considering the experiment, the close to one signal-to-noise ratio in the region of the RBM could be improved, which is important, because in such situations the RBM intensity value might be strongly affected by the emissive background removal procedure. Furthermore, by careful analysis Magg et al. find that the contribution of (10,0) and (9,3) contaminants to the Raman spectrum in the RBM region (around 309 cm^{-1}) is comparable to or even larger than the signal of (6,5) itself (see Figure S2 of ref 30). This effect (easily argued by a stronger resonance enhancement of the contaminants at 532 nm) might have shown up in the ROA spectrum as well, because (9,3) is chiral. Unfortunately our implementation is not suitable for computing the ROA spectrum of the metallic (9,3) tube; we are, therefore, not able to investigate this aspect.

Reliability of our semiempirical approach considering the sign of the RBM ROA signal would also be highly desirable to verify by comparison to more involved theoretical treatments. This is, however, out of the applicability of any program available presently. Such an efficient and accurate implementation would probably require the full exploitation of helical

symmetry at least at the DFT level of theory, like it has been reported recently by Dovesi et al. for the case of dipole polarizabilities.[117] An alternative line of improvement could be to include vibronic detail in the formulation of the ROA polarizability tensors,[66−68] as it is not the 532 nm laser frequency but the Stokes-shifted frequency that is found in close resonance with the E$_{22}$ transition of the (6,5) nanotube.[30] Excitation energy values of Table 2 suggest that one cannot assume strong resonance with only one electronic transition for all SWCNTs and generally cannot rely on the single excited state limit.[66] Approaches taking into account a couple of excited states have been proposed for small molecules,[67,68] but their application for SWCNTs is still too demanding.

Returning to the analysis of Figure 3, significant contribution of IFMs to the ROA spectra is observed, which represents a marked difference compared with the Raman spectra. Both the signs and positions of the IFM bands are beneficially diverse, making ROA a promising tool for the identification SWCNTs and derivatives thereof.

Maximal ROA (absolute) intensity values relative to methyloxirane, collected in Table 2, are one or 2 orders of magnitude larger than the same quantities for Raman. This effect can be explained with the structure of chiral SWCNTs. The long helical motif in the arrangement of the carbon atoms can give a large contribution to the ROA signal, whereas the Raman scattering is relatively indifferent to this structural pattern. This observation is in accord with previous studies on hexahelicene derivatives, where the increased ROA signal was attributed to collective carbon skeleton vibrational motions of extended helical structural elements.[118,119]

Similar to the Raman effect, ROA intensities also depend strongly on the incident light frequency. The interesting new feature of the resonance ROA profile of the (6,5) tube, depicted in Figure 4, is the sign change for all major peaks as ω passes
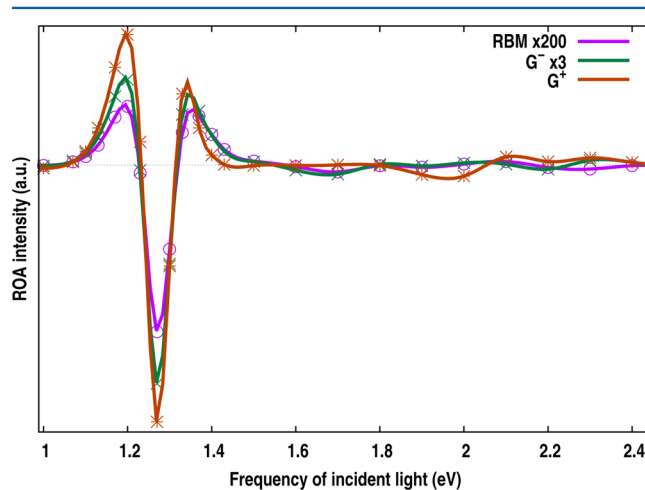
Figure 4. Resonance ROA profile of SWCNT (6,5) using the TB approximation. The RBM intensity is scaled by a factor of 200, and G$^-$ is multiplied by 3 to match the magnitude of G$^+$.

through the first excitation energy. This opens a possibility to distinguish overlapping bands (for instance in the region of the most intense G$^+$ mode) in a mixed sample, using a well chosen incident light frequency. In contrast with resonance Raman curves, enhancement originating from resonance with the $1 \rightarrow$ 2 or $2 \rightarrow 2$ electronic transitions cannot be observed clearly in

Figure 4. The strongest ROA signal is, therefore, expected from resonance with the first electronic transition.

In accord with our previous prediction,[29] Magg et al.[30] provide experimental evidence in the case of the (6,5) tube that SWCNTs can indeed exhibit remarkably strong Raman and ROA signals. Inspecting Table 2, the same theoretical prediction holds for all six investigated nanotubes. (Note that there are two differences in the computational model used for the nanotubes and the methyloxirane spectra, the latter being the reference in Table 2. First, it was possible to employ a much more sophisticated computational model for methyloxirane. Second, the comparison is made with 532 nm incident light where resonance occurs only in the case of the nanotubes. However, our aim was to estimate the methyloxirane spectra with the experimentally most relevant 532 nm as well as possible, because it is frequently measured, and to compare the strength of the estimated nanotube ROA signal to that reliable reference.)

On the basis of a previous analysis,[29,63] we judge that Raman and ROA cross sections obtained by the present computational protocol are overestimated by a rough factor of 100−1000, which mainly originates from the error of the TB model compared to DFT. Relative ROA intensities of Table 2 are accordingly expected to be on the order of 10^5−10^6 in practice (in contrast to the 10^8−10^9 values suggested by Table 2). For comparison, the same relative intensity (with respect to methyloxirane) is just 10^3−10^4 in the case of chiral full-erenes.[29,62] The exceptionally strong ROA signal of SWCNTs compared to the effect produced by small molecules at the same incident light frequency can be attributed both to the resonance enhancement and to the extended helical pattern of the chiral nanotubes.

4. CONCLUSION AND OUTLOOK

Theoretical resonance Raman and ROA spectra of chiral SWCNTs are reported, on the basis of the combination of scattering tensors computed at the π-electron level with DFT vibrational modes. Comparison with the recent experimental ROA spectrum of the (6,5) tube[30] represents further validation of the present computational protocol, in addition to previous assessments based on chiral fullerenes.[29,62,63] The theoretical model applied here improves upon our previous studies in the following: (i) level shifts according to eq 24 are used to correct for one-particle electronic energy differences; (ii) band polarization terms are included when matrix elements of multipole operators are computed (cf. eq 30). Periodic forms for the magnetic dipole and the electric quadrupole operators are introduced here (eqs 21 and 22) in analogy with the commonly applied periodic electric dipole. Contribution of antisymmetric invariants to Raman and ROA scattering cross sections (cf. eqs 14 and 15) is discussed in detail.

Comparison of the theoretical spectrum for the (6,5) nanotube with the experiment of ref 30 reveals good agreement in terms of both sign and relative intensity for all bands, except for the signal sign of the radial breathing mode. This disagreement cannot be resolved on the basis of the data available to us presently and requires further investigation.

Besides the recently measured (6,5) tube, ROA spectra of five more chiral SWCNTs are presented. These may aid forthcoming experiments in absolute configuration determination. Notable contribution of the fundamental intermediate frequency modes is a common feature of computed ROA spectra. This represents an enrichment compared to Raman

that may assist nanotube identification. On the basis of the computations, we judge that the ROA signal of chiral SWCNTs is at least 5−6 orders of magnitude stronger than that of commonly measured small, organic compounds. The reason for this is the resonance enhancement on the one hand and the uniquely long helical arrangement of the carbon atoms of the chiral SWCNTs on the other hand. Resonance ROA profile of the (6,5) tube shows an interesting sign change in the region of the first electronic excitation. This might also be exploited for experimental identification of components of a nanotube mixture.

The magnitude of resonance enhancement in the case of Raman and ROA of SWCNTs is comparable. This may motivate extension of well-developed techniques of Raman microscopy to the field of ROA. Among other related chiral structures, multilayer graphenes and multiwalled nanotubes can also exhibit ROA if the mirror planes of their (achiral) monomers are not coinciding.

■ APPENDIX A. CONNECTION OF $\hat{M}$ TO MTOM

The MTOM formula for the orbital magnetization of nonmetallic systems can be expressed with the following matrix element of the magnetic moment:[84]

$$(M_\alpha)_{jj}(\mathbf{k}) = -\frac{i}{2}\epsilon_{\alpha\beta\gamma}\langle\nabla_{k_\beta}u_j(\mathbf{k,r})|\overline{H}(\mathbf{k})|\nabla_{k_\gamma}u_j(\mathbf{k,r})\rangle \quad (25)$$

with $\overline{H}(\mathbf{k}) = e^{-i\mathbf{kr}}He^{i\mathbf{kr}}$ and $u_j(\mathbf{k,r})$ denoting the periodic part of the COs of eq 4, i.e., $\varphi_j(\mathbf{k,r}) = e^{i\mathbf{kr}}u_j(\mathbf{k,r})$.

In comparison, the analogous matrix elements of the periodic magnetic dipole operator, $\hat{M}$ of eq 21, with COs reads

$$(\mathcal{M}_\alpha)_{jj}(\mathbf{k}) = -\frac{1}{2}\epsilon_{\alpha\beta\gamma}\langle u_j(\mathbf{k,r})e^{i\mathbf{kr}}|\mathcal{R}_\beta p_\gamma|e^{i\mathbf{kr}}u_j(\mathbf{k,r})\rangle \quad (26)$$

Let us proceed with the substitution of $\mathcal{R}_\beta = ie^{i\mathbf{kr}}\nabla_{k_\beta}e^{-i\mathbf{kr}}$ and of the EOM of periodic systems (eq 23) into the above magnetic dipole formula:

$$(\mathcal{M}_\alpha)_{jj}(\mathbf{k}) = -\frac{i}{2}\epsilon_{\alpha\beta\gamma}(\langle u_j(\mathbf{k,r})|\nabla_{k_\beta}e^{-i\mathbf{kr}}He^{i\mathbf{kr}}\nabla_{k_\gamma}|u_j(\mathbf{k,r})\rangle$$
$$- \langle u_j(\mathbf{k,r})|\nabla_{k_\beta}\nabla_{k_\gamma}e^{-i\mathbf{kr}}H|e^{i\mathbf{kr}}u_j(\mathbf{k,r})\rangle) \quad (27)$$

One can exploit the Schrödinger equation in the second term of the right-hand side as

$$H|e^{i\mathbf{kr}}u_j(\mathbf{k,r})\rangle = \varepsilon_j(\mathbf{k})|e^{i\mathbf{kr}}u_j(\mathbf{k,r})\rangle$$

and recognize that the resulting expression cancels, because

$$\epsilon_{\alpha\beta\gamma}\varepsilon_j(\mathbf{k})\langle\nabla_{k_\beta}u_j(\mathbf{k,r})|\nabla_{k_\gamma}u_j(\mathbf{k,r})\rangle = 0$$

due to the properties of the cross product.

Finally, one finds the first term on the right-hand side of eq 27 is in complete agreement with the corresponding MTOM expression in eq 25.

■ APPENDIX B. MATRIX ELEMENTS OF MULTIPOLE OPERATORS

The zero differential overlap (ZDO) approximation is applied for matrix elements of the multipole operators of section 2.3 taken with the basis functions of eq 2. Within the ZDO approximation any multiplicative operator takes the matrix element

$$\langle \phi_\mu(k,\mathbf{r})|A|\phi_\nu(k',\mathbf{r})\rangle = A_{\mu\mu}(k)\delta_{\mu\nu}\delta_{kk'} \tag{28}$$

The above treatment of multipoles is consistent with the TB model Hamiltonian.

Considering the occupied-virtual matrix element of the electric dipole, conventional techniques[120,121] lead to the result

$$(d_\alpha)_{ja}(k) = -\sum_{\mu,\nu} C^*_{\mu j}(k)\left[(\hat{r}_\alpha)_{\mu\nu} + \mathrm{i}\langle\phi_\mu(k,\mathbf{r})|\frac{\partial}{\partial k}|\phi_\nu(k,\mathbf{r})\rangle\right.$$
$$\left. + \mathrm{i}S_{\mu\nu}(k)\frac{\partial}{\partial k}\right]C_{\nu a}(k)$$
$$= -\sum_\mu C^*_{\mu j}(k)(R_\alpha)_\mu C_{\mu a}(k) + \mathrm{i}U_{ja}(k) \tag{29}$$

where $S_{\mu\nu}(k) = \delta_{\mu\nu}$ is the overlap matrix of the symmetry adapted basis of eq 2, $(R_\alpha)_\mu$ is the α coordinate of atom μ in the reference unit cell and the CO derivatives with respect to k, i.e.

$$\frac{\partial}{\partial k}C_{\mu a}(k) = \sum_{p\neq a} U_{pa}(k)\,C_{\mu p}(k) \tag{30}$$

are determined relying on the (coupled)perturbed approach.[120,121] Let us note again that this so-called band polarization term, which depends on $U_{ja}(k)$, was not included in our previous report;[29] hence, the present ROA spectrum of the (6,5) nanotube differs from the one in ref 29.

Matrix elements of the magnetic dipole operator can be expressed with the corresponding components of the coordinate and momentum operator after inserting the resolution of identity in the CO basis between operators $\hat{R}$ and $\hat{\mathbf{p}}$:

$$(m_\alpha)_{ja}(k) = (\hat{\mathcal{M}}_\alpha)_{ja}(k) = \frac{\epsilon_{\alpha\beta\gamma}}{2}\sum_q (d_\beta)_{jq}(k)(p_\gamma)_{qa}(k) \tag{31}$$

where the momentum matrix elements are obtained via the periodic EOM of eq 23 as

$$(p_\gamma)_{qa}(k) = \mathrm{i}[\varepsilon_a(k) - \varepsilon_q(k)](d_\gamma)_{qa}(k) \tag{32}$$

Analogously, the CO matrix elements of the electric quadrupole operator read

$$(\Theta_{\alpha\beta})_{ja}(k) = (\hat{\mathcal{T}}_{\alpha\beta})_{ja}(k) = \frac{1}{2}\sum_s [3(d_\alpha)_{js}(k)(d_\beta)_{sa}(k)$$
$$- \delta_{\alpha\beta}\sum_\lambda (d_\lambda)_{js}(k)(d_\lambda)_{sa}(k)] \tag{33}$$

■ AUTHOR INFORMATION

Corresponding Author

*P. Nagy. E-mail: nagyrpeter@mail.bme.hu. Phone: +36 (1) 463-1632.

Notes

The authors declare no competing financial interest.

■ ACKNOWLEDGMENTS

■ REFERENCES

(1) Hidalgo, F.; Noguez, C. Optically Active Nanoparticles: Fullerenes, Carbon Nanotubes, and Metal Nanoparticles. *Phys. Status Solidi B* **2010**, *247*, 1889−1897.

(2) Chen, X.-Q.; Liao, X.-Y.; Yu, J.-G.; Jiao, F.-P.; Jiang, X.-Y. Chiral Carbon Nanotubes and Carbon Nanotube Chiral Composites: Preparation and Applications. *Nano* **2013**, *08*, 1330002.

(3) Prasek, J.; Drbohlavova, J.; Chomoucka, J.; Hubalek, J.; Jasek, O.; Adam, V.; Kizek, R. Methods for Carbon Nanotubes Synthesis-Review. *J. Mater. Chem.* **2011**, *21*, 15872−15884.

(4) Reich, S.; Thomsen, C.; Maultzsch, J. *Carbon Nanotubes: Basic Concepts and Physical Properties*; Wiley: Hoboken, NJ, 2004.

(5) Damnjanović, M.; Milošević, I.; Dobardžić, E.; Vuković, T.; Nikolić, B. In *Applied Physics of Carbon Nanotubes: Fundamentals of Theory, Optics and Transport Devices*; Rotkin, S. V., Subramoney, S., Eds.; Springer Science & Business Media: Berlin, 2006.

(6) Komatsu, N.; Wang, F. *Materials* **2010**, *3*, 3818−3844.

(7) Peng, X.; Komatsu, N.; Bhattacharya, S.; Shimawaki, T.; Aonuma, S.; Kimura, T.; Osuka, A. Optically Active Single-Walled Carbon Nanotubes. *Nat. Nanotechnol.* **2007**, *2*, 361−365.

(8) Peng, X.; Wang, F.; Bauri, A. K.; Rahman, A. F. M. M.; Komatsu, N. Optical Resolution of Single-Walled Carbon Nanotubes Through Molecular Recognition with Chiral Diporphyrin Nanotweezers. *Chem. Lett.* **2010**, *39*, 1022−1027.

(9) Pérez, E. M.; Martín, N. Chiral Recognition of Carbon Nanoforms. *Org. Biomol. Chem.* **2012**, *10*, 3577−3583.

(10) Klärner, F.-G.; Schrader, T. Aromatic Interactions by Molecular Tweezers and Clips in Chemical and Biological Systems. *Acc. Chem. Res.* **2013**, *46*, 967−978.

(11) Zheng, M.; Semke, E. D. Enrichment of Single Chirality Carbon Nanotubes. *J. Am. Chem. Soc.* **2007**, *129*, 6084−6085.

(12) Akazaki, K.; Toshimitsu, F.; Ozawa, H.; Fujigaya, T.; Nakashima, N. Recognition and One-Pot Extraction of Right- and Left-Handed Semiconducting Single-Walled Carbon Nanotube Enantiomers Using Fluorene-Binaphthol Chiral Copolymers. *J. Am. Chem. Soc.* **2012**, *134*, 12700−12707.

(13) Wang, F.; Matsuda, K.; Rahman, A. F. M. M.; Kimura, T.; Komatsu, N. Improved Selectivity in Discriminating Handedness and Diameter of Single-Walled Carbon Nanotubes with N-Substituted 3,6-Carbazolylene-Bridged Chiral Diporphyrin Nanotweezers. *Nanoscale* **2011**, *3*, 4117−4124.

(14) Liu, G.; Wang, F.; Chaunchaiyakul, S.; Saito, Y.; Bauri, A. K.; Kimura, T.; Kuwahara, Y.; Komatsu, N. Simultaneous Discrimination of Diameter, Handedness, and Metallicity of Single-Walled Carbon Nanotubes with Chiral Diporphyrin Nanocalipers. *J. Am. Chem. Soc.* **2013**, *135*, 4805−4814.

(15) Green, A.; Duch, M.; Hersam, M. Isolation of Single-Walled Carbon Nanotube Enantiomers by Density Differentiation. *Nano Res.* **2009**, *2*, 69−77.

(16) Ghosh, S.; Bachilo, S. M.; Weisman, R. B. Advanced Sorting of Single-Walled Carbon Nanotubes by Nonlinear Density-Gradient Ultracentrifugation. *Nat. Nanotechnol.* **2010**, *5*, 443−450.

(17) Liu, H.; Nishide, D.; Tanaka, T.; Kataura, H. Large-Scale Single-Chirality Separation of Single-Wall Carbon Nanotubes by Simple Gel Chromatography. *Nat. Commun.* **2011**, *2*, 309.

(18) Fagan, J. A.; Hároz, E. H.; Ihly, R.; Gui, H.; Blackburn, J. L.; Simpson, J. R.; Lam, S.; Hight Walker, A. R.; Doorn, S. K.; Zheng, M. Isolation of > 1 nm Diameter Single-Wall Carbon Nanotube Species Using Aqueous Two-Phase Extraction. *ACS Nano* **2015**, *9*, 5377−5390.

(19) Scott, L. T.; Jackson, E. A.; Zhang, Q.; Steinberg, B. D.; Bancu, M.; Li, B. A Short, Rigid, Structurally Pure Carbon Nanotube by Stepwise Chemical Synthesis. *J. Am. Chem. Soc.* **2012**, *134*, 107−110.

(20) Liu, J.; Wang, C.; Tu, X.; Liu, B.; Chen, L.; Zheng, M.; Zhou, C. Chirality-Controlled Synthesis of Single-Wall Carbon Nanotubes Using Vapour-Phase Epitaxy. *Nat. Commun.* **2012**, *3*, 1199.

(21) Li, H.-B.; Page, A. J.; Irle, S.; Morokuma, K. Single-Walled Carbon Nanotube Growth from Chiral Carbon Nanorings: Prediction of Chirality and Diameter Influence on Growth Rates. *J. Am. Chem. Soc.* **2012**, *134*, 15887−15896.

(22) Peng, X.; Komatsu, N.; Kimura, T.; Osuka, A. Improved Optical Enrichment of SWNTs Through Extraction with Chiral Nanotweezers of 2,6-Pyridylene-Bridged Diporphyrins. *J. Am. Chem. Soc.* **2007**, *129*, 15947−15953.

(23) Peng, X.; Komatsu, N.; Osuka, A. Simultaneous Enrichments of Optical Purity and (n,m) Abundance of SWNTs Through Extraction with 3,6- Carbazolylene-Bridged Chiral Diporphyrin Nanotweezers. *ACS Nano* **2008**, *2*, 2045−2050.

(24) Ghosh, S.; Bachilo, S. M.; Weisman, R. B. Structure-Dependent Optical Activity of Single-Walled Carbon Nanotube Enantiomers. *Fullerenes, Nanotubes, Carbon Nanostruct.* **2014**, *22*, 269−279.

(25) Samsonidze, G. G.; Grüneis, A.; Saito, R.; Jorio, A.; Souza Filho, A. G.; Dresselhaus, G.; Dresselhaus, M. S. Interband Optical Transitions in Left- and Right-Handed Single-Wall Carbon Nanotubes. *Phys. Rev. B: Condens. Matter Mater. Phys.* **2004**, *69*, 205402.

(26) Sánchez-Castillo, A.; Román-Velázquez, C. E.; Noguez, C. Optical Circular Dichroism of Single-Wall Carbon Nanotubes. *Phys. Rev. B: Condens. Matter Mater. Phys.* **2006**, *73*, 045401.

(27) Hidalgo, F.; Sánchez-Castillo, A.; Noguez, C. Efficient First-Principles Method for Calculating the Circular Dichroism of Nanostructures. *Phys. Rev. B: Condens. Matter Mater. Phys.* **2009**, *79*, 075438.

(28) Sánchez-Castillo, A.; Noguez, C. Understanding Optical Activity in Single-Walled Carbon Nanotubes from First-Principles Studies. *J. Phys. Chem. C* **2010**, *114*, 9640−9644.

(29) Nagy, P. R.; Biró, L.; Koltai, J.; Surján, P. R.; Szabados, Á; Kürti, J. Theoretical Vibrational Optical Activity of Chiral Carbon Nanoparticles: Fullerenes and Carbon Nanotubes. *Phys. Status Solidi B* **2014**, *251*, 2451−2456.

(30) Magg, M.; Kadria-Vili, Y.; Oulevey, P.; Weisman, R. B.; Bürgi, T. Resonance Raman Optical Activity Spectra of Single-Walled Carbon Nanotube Enantiomers. *J. Phys. Chem. Lett.* **2016**, *7*, 221−225.

(31) Wilder, J. W. G.; Venema, L. C.; Rinzler, A. G.; Smalley, R. E.; Dekker, C. Electronic Structure of Atomically Resolved Carbon Nanotubes. *Nature* **1998**, *391*, 59−62.

(32) Odom, T. W.; Huang, J.-L.; Kim, P.; Lieber, C. M. Atomic Structure and Electronic Properties of Single-Walled Carbon Nanotubes. *Nature* **1998**, *391*, 62−64.

(33) Liu, Z.; Suenaga, K.; Yoshida, H.; Sugai, T.; Shinohara, H.; Iijima, S. Determination of Optical Isomers for Left-Handed or Right-Handed Chiral Double-Wall Carbon Nanotubes. *Phys. Rev. Lett.* **2005**, *95*, 187406.

(34) Nafie, L. A. *Vibrational Optical Activity: Principles and Applications*; John Wiley & Sons: Hoboken, NJ, 2011.

(35) Barron, L. D. *Molecular Light Scattering and Optical Activity*; Cambridge University Press: Cambridge, U.K., 2004.

(36) Barron, L. D.; Buckingham, A. D. Vibrational Optical Activity. *Chem. Phys. Lett.* **2010**, *492*, 199−213.

(37) Dresselhaus, M.; Jorio, A.; Saito, R. Characterizing Graphene, Graphite, and Carbon Nanotubes by Raman Spectroscopy. *Annu. Rev. Condens. Matter Phys.* **2010**, *1*, 89−108.

(38) Thorvaldsen, A. J.; Gao, B. I. N.; Ruud, K.; Fedorovsky, M.; Zuber, G.; Hug, W. Efficient Calculation of ROA Tensors with Analytical Gradients and Fragmentation. *Chirality* **2012**, *24*, 1018−1030.

(39) Kaledin, A. L. Gradient-Based Direct Normal-Mode Analysis. *J. Chem. Phys.* **2005**, *122*, 184106.

(40) Weymuth, T.; Haag, M. P.; Kiewisch, K.; Luber, S.; Schenk, S.; Jacob, C. R.; Herrmann, C.; Neugebauer, J.; Reiher, M. MOVIPAC: Vibrational Spectroscopy with a Robust Meta-Program for Massively Parallel Standard and Inverse Calculations. *J. Comput. Chem.* **2012**, *33*, 2186−2198.

(41) Kussmann, J.; Luenser, A.; Beer, M.; Ochsenfeld, C. a Reduced-Scaling Density Matrix-Based Method for the Computation of the Vibrational Hessian Matrix at the Self-Consistent Field Level. *J. Chem. Phys.* **2015**, *142*, 094101.

(42) Koltai, J.; Zólyomi, V.; Kürti, J. Phonon Dispersion of Small Diameter Semiconducting Chiral Carbon Nanotubes-A Theoretical Study. *Phys. Status Solidi B* **2008**, *245*, 2137−2140.

(43) Zólyomi, V.; Koltai, J.; Kürti, J.; Kuzmany, H. In *DFT Calculations on Fullerenes and Carbon Nanotubes*; Basiuk, V., Irle, S., Eds.; Signpost Publisher: Kerala, India, 2008.

(44) Ruud, K.; Thorvaldsen, A. J. Theoretical Approaches to the Calculation of Raman Optical Activity Spectra. *Chirality* **2009**, *21*, 54−67.

(45) Liégeois, V.; Ruud, K.; Champagne, B. An Analytical Derivative Procedure for the Calculation of Vibrational Raman Optical Activity Spectra. *J. Chem. Phys.* **2007**, *127*, 204105.

(46) Pecul, M.; Ruud, K. Ab Initio Calculation of Vibrational Raman Optical Activity. *Int. J. Quantum Chem.* **2005**, *104*, 816−829.

(47) Pecul, M. New Applications and Challenges for Computational ROA Spectroscopy. *Chirality* **2009**, *21*, 98−104.

(48) Polavarapu, P. L. Quantum Mechanical Predictions of Chiroptical Vibrational Properties. *Int. J. Quantum Chem.* **2006**, *106*, 1809−1814.

(49) Crawford, T. D. Ab Initio Calculation of Molecular Chiroptical Properties. *Theor. Chem. Acc.* **2006**, *115*, 227−245.

(50) Autschbach, J. Computing Chiroptical Properties with First-Principles Theoretical Methods: Background and Illustrative Examples. *Chirality* **2009**, *21*, 116−152.

(51) Luber, S.; Reiher, M. Theoretical Raman Optical Activity Study of the Beta Domain of Rat Metallothionein. *J. Phys. Chem. B* **2010**, *114*, 1057−1063.

(52) Yamamoto, S.; Li, X.; Ruud, K.; Bouř, P. Transferability of Various Molecular Property Tensors in Vibrational Spectroscopy. *J. Chem. Theory Comput.* **2012**, *8*, 977−985.

(53) Jose, K. V. J.; Raghavachari, K. Raman Optical Activity Spectra for Large Molecules Through Molecules-In-Molecules Fragment-Based Approach. *J. Chem. Theory Comput.* **2016**, *12*, 585−594.

(54) Cheeseman, J. R.; Frisch, M. J. Basis Set Dependence of Vibrational Raman and Raman Optical Activity Intensities. *J. Chem. Theory Comput.* **2011**, *7*, 3323−3334.

(55) Jensen, L.; Autschbach, J.; Krykunov, M.; Schatz, G. C. Resonance Vibrational Raman Optical Activity: A Time-Dependent Density Functional Theory Approach. *J. Chem. Phys.* **2007**, *127*, 134101.

(56) Otto, P. Calculation of the Polarizability and Hyperpolarizabilities of Periodic Quasi-One-Dimensional Systems. *Phys. Rev. B: Condens. Matter Mater. Phys.* **1992**, *45*, 10876−10885.

(57) Maschio, L.; Kirtman, B.; Rérat, M.; Orlando, R.; Dovesi, R. Ab Initio Analytical Raman Intensities for Periodic Systems Through a Coupled Perturbed Hartree-Fock/Kohn-Sham Method in an Atomic Orbital Basis. I. Theory. *J. Chem. Phys.* **2013**, *139*, 164101.

(58) Putrino, A.; Parrinello, M. Anharmonic Raman Spectra in High-Pressure Ice from Ab Initio Simulations. *Phys. Rev. Lett.* **2002**, *88*, 176401.

(59) Lazzeri, M.; Mauri, F. First-Principles Calculation of Vibrational Raman Spectra in Large Systems: Signature of Small Rings in Crystalline SiO_2. *Phys. Rev. Lett.* **2003**, *90*, 036401.

(60) Hecht, L.; Nafie, L. A. Theory of Natural Raman Optical Activity Part I. Complete Circular Polarization Formalizm. *Mol. Phys.* **1991**, *72*, 441−469.

(61) Nafie, L. A.; D, C. *Advances in Chemical Physics*; Wiley: Hoboken, NJ, 1993; Vol. *85*, Part 3, pp 105−149.

(62) Nagy, P. R.; Surján, P. R.; Szabados, Á Vibrational Optical Activity of Chiral Carbon Nanoclusters Treated by a Generalized π-Electron Method. *J. Chem. Phys.* **2014**, *140*, 044112.

(63) Nagy, P. R. Theoretical Developments and Computational Studies in Chiroptical Spectroscopies. *Ph.D. Dissertation*, DOI 10.15476/ELTE.2015.010; Eötvös University, 2015.

(64) Kürti, J.; Surján, P. R. Embedded Units in Conjugated Polymers. *J. Math. Chem.* **1992**, *10*, 313−327.

(65) Surján, P. R.; Lázár, A.; Kállay, M. Electronic Structure of the Singly Bonded $(C_{60})_x$ Fullerene Polymer. *Phys. Rev. B: Condens. Matter Mater. Phys.* **1998**, *58*, 3490.

(66) Nafie, L. A. Theory of Resonance Raman Optical Activity: The Single Electronic State Limit. *Chem. Phys.* **1996**, *205*, 309−322.

(67) Luber, S.; Neugebauer, J.; Reiher, M. Enhancement and De-Enhancement Effects in Vibrational Resonance Raman Optical Activity. *J. Chem. Phys.* **2010**, *132*, 044113.

(68) Merten, C.; Li, H.; Nafie, L. A. Simultaneous Resonance Raman Optical Activity Involving Two Electronic States. *J. Phys. Chem. A* **2012**, *116*, 7329−7336.

(69) Nafie, L. A. Infrared and Raman Vibrational Optical Activity: Theoretical and Experimental Aspects. *Annu. Rev. Phys. Chem.* **1997**, *48*, 357−386.

(70) Nafie, L. A. Theory of Raman Scattering and Raman Optical Activity: Near Resonance Theory and Levels of Approximation. *Theor. Chem. Acc.* **2008**, *119*, 39−55.

(71) Blount, E. In *Formalisms of Band Theory*; Seitz, F., Turnbull, D., Eds.; Solid State Physics; Academic Press: London, 1962; Vol. *13*, pp 305−373.

(72) Wannier, G. H. Dynamics of Band Electrons in Electric and Magnetic Fields. *Rev. Mod. Phys.* **1962**, *34*, 645−655.

(73) Kittel, C. *Quantum theory of solids*; Wiley: Hoboken, NJ, 1963.

(74) Luber, S. Exploring Raman Optical Activity for Transition Metals: From Coordination Compounds to Solids. *Biomed. Spectrosc. Imaging* **2015**, *4*, 255−268.

(75) Champagne, B.; Bishop, D. M. *Advances in Chemical Physics*; John Wiley & Sons, Inc.: Hoboken, NJ, 2003; pp 41−92.

(76) Izmaylov, A. F.; Brothers, E. N.; Scuseria, G. E. Linear-Scaling Calculation of Static and Dynamic Polarizabilities in Hartree-Fock and Density Functional Theory for Periodic Systems. *J. Chem. Phys.* **2006**, *125*, 224105.

(77) Springborg, M.; Kirtman, B. Analysis of Vector Potential Approach for Calculating Linear and Nonlinear Responses of Infinite Periodic Systems to a Finite Static External Electric Field. *Phys. Rev. B: Condens. Matter Mater. Phys.* **2008**, *77*, 045102.

(78) Dovesi, R.; Orlando, R.; Erba, A.; Zicovich-Wilson, C. M.; Civalleri, B.; Casassa, S.; Maschio, L.; Ferrabone, M.; De La Pierre, M.; D'Arco, P.; et al. CRYSTAL14: A Program for the Ab Initio Investigation of Crystalline Solids. *Int. J. Quantum Chem.* **2014**, *114*, 1287−1317.

(79) Krieger, J.; Iafrate, G. Time Evolution of Bloch Electrons in a Homogeneous Electric Field. *Phys. Rev. B: Condens. Matter Mater. Phys.* **1986**, *33*, 5494−5500.

(80) Kirtman, B.; Gu, F. L.; Bishop, D. M. Extension of the Genkin and Mednis Treatment for Dynamic Polarizabilities and Hyperpolarizabilities of Infinite Periodic Systems. I. Coupled Perturbed Hartree-Fock Theory. *J. Chem. Phys.* **2000**, *113*, 1294.

(81) Resta, R. Theory of the Electric Polarization in Crystals. *Ferroelectrics* **1992**, *136*, 51−55.

(82) Resta, R. Manifestations of Berry's Phase in Molecules and Condensed Matter. *J. Phys.: Condens. Matter* **2000**, *12*, R107−R143.

(83) Kudin, K. N.; Scuseria, G. E. An Efficient Finite Field Approach for Calculating Static Electric Polarizabilities of Periodic Systems. *J. Chem. Phys.* **2000**, *113*, 7779.

(84) Resta, R.; Ceresoli, D.; Thonhauser, T.; Vanderbilt, D. Orbital Magnetization in Extended Systems. *ChemPhysChem* **2005**, *6*, 1815−1819.

(85) Thonhauser, T.; Ceresoli, D.; Vanderbilt, D.; Resta, R. Orbital Magnetization in Periodic Insulators. *Phys. Rev. Lett.* **2005**, *95*, 137205.

(86) Rérat, M.; Ferrero, M.; Amzallag, E.; Baraille, I.; Dovesi, R. Comparison of the Polarizability of Periodic Systems Computed by Using the Length and Velocity Operators. *JPCS* **2008**, *117*, 012023.

(87) Gajdoš, M.; Hummer, K.; Kresse, G.; Furthmüller, J.; Bechstedt, F. Linear Optical Properties in the Projector-Augmented Wave Methodology. *Phys. Rev. B: Condens. Matter Mater. Phys.* **2006**, *73*, 045112.

(88) Hidalgo, F.; Sánchez-Castillo, A.; Noguez, C. Efficient First-Principles Method for Calculating the Circular Dichroism of Nanostructures. *Phys. Rev. B: Condens. Matter Mater. Phys.* **2009**, *79*, 075438.

(89) Baroni, S.; Resta, R. Ab Initio Calculation of the Macroscopic Dielectric Constant in Silicon. *Phys. Rev. B: Condens. Matter Mater. Phys.* **1986**, *33*, 7017.

(90) Adolph, B.; Gavrilenko, V.; Tenelsen, K.; Bechstedt, F.; Del Sole, R. Nonlocality and Many-Body Effects in the Optical Properties of Semiconductors. *Phys. Rev. B: Condens. Matter Mater. Phys.* **1996**, *53*, 9797−9808.

(91) White, C. T.; Mintmire, J. W. Fundamental Properties of Single-Wall Carbon Nanotubes. *J. Phys. Chem. B* **2005**, *109*, 52−65.

(92) Szakács, P.; Mukherjee, D.; Das, S.; Surján, P. R. Effective π-Electron Hamiltonian for Small-Radii Nanotubes: Novel Interpretation of Curvature-Induced Conductivity of the (5,0) Carbon Nanotube. *Phys. Rev. B: Condens. Matter Mater. Phys.* **2008**, *77*, 193407.

(93) Kresse, G.; Hafner, J. *Ab Initio* Molecular Dynamics for Liquid Metals. *Phys. Rev. B: Condens. Matter Mater. Phys.* **1993**, *47*, 558−561.

(94) Damnjanović, M.; Milošević, I.; Vuković, T.; Sredanović, R. Full Symmetry, Optical Activity, and Potentials of Single-Wall and Multiwall Nanotubes. *Phys. Rev. B: Condens. Matter Mater. Phys.* **1999**, *60*, 2728−2739.

(95) Damnjanovic, M.; Milosevic, I. *Lecture Notes in Physics*; Springer: Berlin, 2010; Vol. *801*.

(96) Rusznyák, Á; Koltai, J.; Zólyomi, V.; Kürti, J. Using Line Group Theory for the Symmetry Assignment of the Phonons of Single Walled Carbon Nanotubes. *Phys. Status Solidi B* **2009**, *246*, 2614−2617.

(97) Cui, C. X.; Kertész, M. Quantum Mechanical Oligomer Approach for the Calculation of Vibrational Spectra of Polymers. *J. Chem. Phys.* **1990**, *93*, 5257−5266.

(98) Vuković, T.; Milošević, I.; Damnjanović, M. Carbon Nanotubes Band Assignation, Topology, Bloch States, and Selection Rules. *Phys. Rev. B: Condens. Matter Mater. Phys.* **2002**, *65*, 045418.

(99) Alon, O. E. Number of Raman- and Infrared-Active Vibrations in Single-Walled Carbon Nanotubes. *Phys. Rev. B: Condens. Matter Mater. Phys.* **2001**, *63*, 201403.

(100) Alon, O. E. from Spatial Symmetry to Vibrational Spectroscopy of Single-Walled Nanotubes. *J. Phys.: Condens. Matter* **2003**, *15*, S2489−S2500.

(101) Alvarez, L.; Righi, A.; Rols, S. Excitation Energy Dependence of the Raman Spectrum of Single-Walled Carbon Nanotubes. *Chem. Phys. Lett.* **2000**, *320*, 441−447.

(102) Fantini, C.; Jorio, A.; Souza, M.; Ladeira, L.; Souza Filho, A.; Saito, R.; Samsonidze, G.; Dresselhaus, G.; Dresselhaus, M.; Pimenta, M. One-Dimensional Character of Combination Modes in the Resonance Raman Scattering of Carbon Nanotubes. *Phys. Rev. Lett.* **2004**, *93*, 087401.

(103) Singh, D. K.; Iyer, P. K.; Giri, P. K. Distinguishing Defect Induced Intermediate Frequency Modes from Combination Modes in the Raman Spectrum of Single Walled Carbon Nanotubes. *J. Appl. Phys.* **2012**, *111*, 064304.

(104) Wang, J.; Yang, J.; Zhang, D.; Li, Y. Structure Dependence of the Intermediate-Frequency Raman Modes in Isolated Single-Walled Carbon Nanotubes. *J. Phys. Chem. C* **2012**, *116*, 23826−23832.

(105) Lim, Y.-S.; Nugraha, A. R. T.; Cho, S.-J.; Noh, M.-Y.; Yoon, E.-J.; Liu, H.; Kim, J.-H.; Telg, H.; Ha, E. H.; Sanders, G. D.; et al. Ultrafast Generation of Fundamental and Multiple-Order Phonon Excitations in Highly Enriched (6,5) Single-Wall Carbon Nanotubes. *Nano Lett.* **2014**, *14*, 1426−1432.

(106) Rafailov, P. M.; Jantoljak, H.; Thomsen, C. Electronic Transitions in Single-Walled Carbon Nanotubes: A Resonance Raman Study. *Phys. Rev. B: Condens. Matter Mater. Phys.* **2000**, *61*, 16179.

(107) Park, J.; Oyama, Y.; Saito, R.; Izumida, W.; Jiang, J.; Sato, K.; Fantini, C.; Jorio, A.; Dresselhaus, G.; Dresselhaus, M. Raman Resonance Window of Single-Wall Carbon Nanotubes. *Phys. Rev. B: Condens. Matter Mater. Phys.* **2006**, *74*, 165414.

(108) Saito, R.; Hofmann, M.; Dresselhaus, G.; Jorio, A.; Dresselhaus, M. S. Raman Spectroscopy of Graphene and Carbon Nanotubes. *Adv. Phys.* **2011**, *60*, 413−550.

(109) Bachilo, S. M.; Strano, M. S.; Kittrell, C.; Hauge, R. H.; Smalley, R. E.; Weisman, R. B. Structure-Assigned Optical Spectra of Single-Walled Carbon Nanotubes. *Science* **2002**, *298*, 2361−2366.

(110) Haroz, E. H.; Bachilo, S. M.; Weisman, R. B.; Doorn, S. K. Curvature Effects on the E_{33} and E_{44} Exciton Transitions in Semiconducting Single-Walled Carbon Nanotubes. *Phys. Rev. B: Condens. Matter Mater. Phys.* **2008**, *77*, 125405.

(111) Monkhorst, H. J.; Pack, J. D. Special Points for Brillouin-Zone Integrations. *Phys. Rev. B* **1976**, *13*, 5188−5192.

(112) Sebestik, J.; Bour, P. Raman Optical Activity of Methyloxirane Gas and Liquid. *J. Phys. Chem. Lett.* **2011**, *2*, 498−502.

(113) Frisch, M. J.; Trucks, G. W.; Schlegel, H. B.; Scuseria, G. E.; Robb, M. A.; Cheeseman, J. R.; Scalmani, G.; Barone, V.; Mennucci, B.; Petersson, G. A.; et al. *Gaussian 09* Revision C.1; Gaussian Inc.: Wallingford, CT, 2009.

(114) Structure and Phonon Band Structure Database of Common SWCNTs, See http://wigner.elte.hu/~adam/chirality.

(115) Kavan, L.; Frank, O.; Green, A. A.; Hersam, M. C.; Koltai, J.; Zólyomi, V.; Kürti, J.; Dunsch, L. In Situ Raman Spectroelectrochemistry of Single-Walled Carbon Nanotubes: Investigation of Materials Enriched with (6,5) Tubes. *J. Phys. Chem. C* **2008**, *112*, 14179−14187.

(116) Božović, I.; Božović, N.; Damnjanović, M. Optical Dichroism in Nanotubes. *Phys. Rev. B: Condens. Matter Mater. Phys.* **2000**, *62*, 6971−6974.

(117) Demichelis, R.; Noel, Y.; D'Arco, P.; Rerat, M.; Zicovich-Wilson, C. M.; Dovesi, R. Properties of Carbon Nanotubes: An Ab Initio Study Using Large Gaussian Basis Sets and Various DFT Functionals. *J. Phys. Chem. C* **2011**, *115*, 8876−8885.

(118) Liégeois, V.; Champagne, B. Vibrational Raman Optical Activity of π-Conjugated Helical Systems: Hexahelicene and Heterohelicenes. *J. Comput. Chem.* **2009**, *30*, 1261−1278.

(119) Johannessen, C.; Blanch, E. W.; Villani, C.; Abbate, S.; Longhi, G.; Agarwal, N. R.; Tommasini, M.; Lightner, D. A. Raman and ROA Spectra of (−)- and (+)-2-Br-Hexahelicene: Experimental and DFT Studies of a π-Conjugated Chiral System. *J. Phys. Chem. B* **2013**, *117*, 2221−2230.

(120) Barbier, C.; Delhalle, J.; Andre, J.-M. Ab Initio Calculations of Tbe Static Electric Polarizability of Infinite Polymer Chains. *J. Mol. Struct.: THEOCHEM* **1989**, *188*, 299−312.

(121) Ferrero, M.; Rérat, M.; Orlando, R.; Dovesi, R. The Calculation of Static Polarizabilities of 1−3D Periodic Compounds. The Implementation in the CRYSTAL Code. *J. Comput. Chem.* **2008**, *29*, 1450−1459.